Metal Exchange Driven Post-Growth Substitutional Tin doping of 2D WS_2 Crystals Using Chemical Vapor Deposition

*Ren-Jie Chang,[1] Yuewen Sheng,[1] Gyeong Hee Ryu,[1] Nhlakanipho Mkhize,[1] Tongxin Chen,[1] Yang Lu,[1] Jun Chen,[1] Ja Kyung Lee,[1] Harish Bhaskaran,[1] Jamie H. Warner[1]**

[1]Department of Materials, University of Oxford, Parks Road, Oxford, OX1 3PH, United Kingdom

Keywords Chemical vapor deposition (CVD), 2D materials, transition metal dichalcogenides, tungsten disulfide, alloys, doping

*Jamie.Warner@materials.ox.ac.uk

Abstract

Doping of two-dimensional (2D) materials provides them tunable physical properties and widens their applications. Here, we demonstrate a post-growth doping strategy in monolayer and bilayer WS_2 crystals that utilizes a metal exchange mechanism, whereby Sn atoms become substitutional dopants in the W sites by energetically favorable replacement. We achieve this using chemical vapor deposition (CVD) techniques, where high quality grown WS_2 single crystals are first grown and then subsequently reacted with a SnS precursor. Thermal control of the exchange doping mechanism is revealed, indicating that a sufficiently high enough temperature is needed to create the S vacancies that are the initial binding sites for the SnS precursor and metal exchange occurrence. This results in a better control of dopants distribution compared to the tradition all-in-one approach, where dopants are added during the

growth phase. The Sn dopants exhibit an n-type doping behavior in the WS_2 layers based on the decreased threshold gate voltage obtained from transistor device measurements. Annular dark field scanning transmission electron microscopy (ADF-STEM) shows that in bilayer WS_2 the Sn doping occurs only in the top layer, creating vertical bilayer heterostructures with atomic layer doping precision. This post-growth modification opens up ways to selectively dope one layer at a time and construct mixed stoichiometry vertical heterojunctions in bilayer crystals.

Introduction

The discovery of graphene has aroused an upsurge of developing other two-dimensional (2D) materials with complementary electronic properties due to their unique structures, high chemical stability and mechanical flexibility.[1-2] Monolayer transition metal dichalcogenides (TMDs) such as molybdenum disulfide (MoS_2) and tungsten disulfide (WS_2) are the well-known examples of 2D semiconductors.[3] They have sensitive dependence of layer number on their bandgaps and exhibit a transition from indirect bandgap in bulks to direct bandgap in monolayers.[4] With the high absorption coefficient and strong photoresponse,[5-7] they are also considered as candidates with a great potential in the future applications of photodetectors,[8-9] field effect transistors,[10-11] light emitting diodes and solar cells.[12-13] Their strong spin–orbit coupling and long spin/valley lifetime, on the other hand, offer them great advantages in data storage and logic devices with high speed and low power consumption.[14]

In light of Si and III-IV semiconductor technologies over the past few decades, doping engineering of 2D materials appears to be the key techniques to effectively modify the physical properties and expand their functionalities.[15-16] Some metal dopants such as Mn and Fe are predicted to enable the induction of magnetism in the 2D semiconductors.[17-19] It is feasible to control the carrier type through substitution doping of specific metal in the 2D semiconductors.

Nb doped MoS_2, for example, exhibits p-type characteristics,[20] while Re dopants act as electron donors resulting in n-type doping for MoS_2.[21] Tunable bandgap can also be obtained by altering chemical composition in 2D transition metal chalcogenide alloys and has been accomplished in several cases via metal or chalcogen substitutional doping, including $Mo_xW_{(1-x)}S_2$,[22-23] $Mo_xW_{(1-x)}Se_2$,[24] $MoS_{2x}Se_{2(1-x)}$,[25-26] $WS_{2x}Se_{2(1-x)}$,[27-28] $SnS_{2x}Se_{2(1-x)}$,[29] and $ReS_{2x}Se_{2(1-x)}$.[30] In addition, it is viable to conduct phase transformation during the doping process of 2D materials. H phase is reported to be the most stable phase at room temperature for MoS_2 and WS_2, but the co-existence of both H phase and T phase was observed in monolayer $Mo_xW_{(1-x)}S_2$ alloy.[31] Yang et al. also demonstrated that stable T-phase MoS_2 could be acquired when alloying with Re through substitutional doping.[32] Similarly, $MoTe_2$ was experimentally shown to undergo a transition of properties from semiconducting to semimetallic as the chemical composition is varied with the W substitution.[33]

Doping of 2D semiconductors is generally categorized into two types: surface chemical doping and substitutional doping. In the case of surface chemical doping, dopants are placed in contact with the 2D semiconductors by physical or chemical interaction without the structural damage. This is usually achieved by chemical treatment or solvent-based intercalation approach and the choosing of dopants could be versatile including small molecules, ions and particles.[34-36] The doping structure, however, lacks covalent surface bonding between the dopants and TMDs, which may be in a metastable state and unable to maintain the modulated properties eternally. Substitutional doping where part of the lattice sites in the original 2D lattice are exchanged by foreign atoms, in comparison, have been widely adopted for band structure engineering and phase engineering.[37-39] This type of doping is usually achieved by using powder vaporization chemical vapor deposition (CVD) approach and introducing all material precursors together during the growth phase of crystals.[40-41] This all-in-one method can lead to the stable substitutional doping structure, but is challenging to

produce high quality dopants due to the different crystallization temperatures of materials and precursor evaporation rates.

Two-step strategy where the host 2D materials are firstly synthesized with high quality and followed by gentle post treatments is a more promising method to integrate different 2D elements together and obtain stable product with controllable properties. Because chalcogen atoms are generally exposed to the outer surface in 2D TMDs, it is easier to replace them with other anionic heteroatoms such as halogen in the post treatment processes.[42] For example, plasma treatment of TMDs under N_2 or PH_3 exposure results in the implantation of nitrogen and phosphorus respectively in the chalcogen vacancies.[43-44] Likewise, thermal annealing of CVD-grown MoS_2 under the Se atmosphere gives rise to the selenide formation via substitutional doping.[45] This brings to the achievement of MoSSe Janus structures with the top chalcogen layer all occupied with Se through adjusting the selenization temperature.[46-47] In contrast, little reports have explored the metal substitution using post-growth treatments as it is difficult to dope extrinsic metal atoms in the lattice of 2D TMDs after CVD growth. This is because transition metal atoms are generally more stable than chalcogens in TMDs and the encapsulating chalcogen atoms act as blocking layers prohibiting the incorporation of the extrinsic metal element in the post-growth treatments.

Here, we report the post-growth modification of CVD-grown WS_2 with metallic Sn dopants using SnS precursor to achieve a range of Sn:W:S composite 2D materials. This post-growth doping method not only preserves the advantages of scalability from traditional CVD approach,[48-50] but provide a better uniformity control for dopant spatial distribution. Using annular dark field scanning transmission electron microscopy (ADF-STEM) of monolayer and bilayer regions we reveal that the substitutional doping of Sn takes place only from top surface. These results provide an improved route to post-growth doping of pre-formed 2D materials (i.e. WS_2 crystals) with other elements (i.e. Sn) to modulate their structures, broadening doping

strategies beyond traditional methods where all precursors are included at the same time during the growth process. This allows the realization of direct selective layer doping in bilayer crystals and could even expand into more chemically complicated structures.

Results and discussion

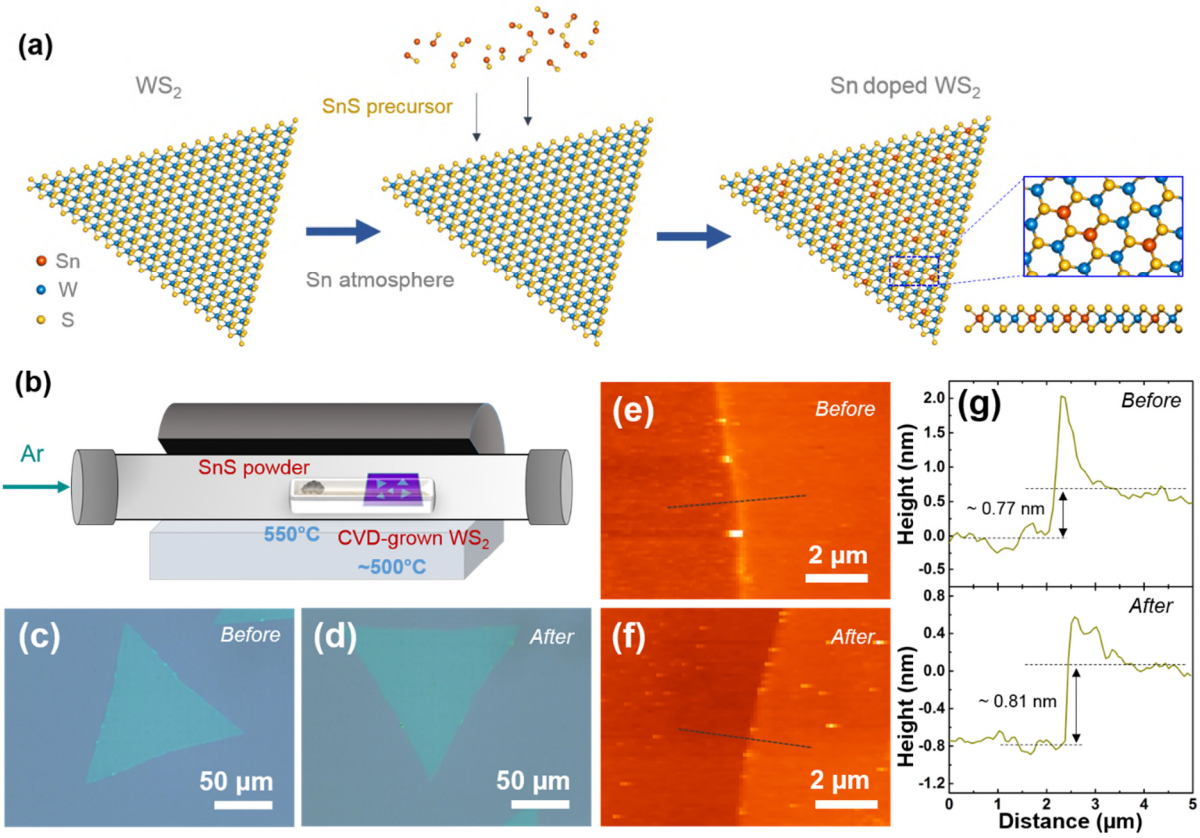

Figure 1. Doping of Sn in the CVD-grown WS_2. (a) Schematics of atomic configuration showing the formation of Sn doped WS_2 monolayers. (b) Schematic illustration of the experimental setup for the thermal doping of Sn in WS_2. (c-d) Optical image of monolayer WS_2 before and after 10 min Sn doping, respectively. (e-f) Atomic force microscopy (AFM) image of monolayer WS_2 before and after 10 min Sn doping, respectively. (g) Line profile from the dark yellow dashed line in (e-f) at the edge corner showing the thickness of WS_2 layers before and after the Sn doping, respectively.

The synthesis of tin-doped WS_2 were employed through a two-step strategy. As shown in Figure 1, the WS_2 monolayers were firstly grown by chemical vapor deposition (CVD) method employing tungsten trioxide (WO_3) and sulfur powders at 1050°C. The presence of WS_2 crystals and their optical properties were examined by Raman and photoluminescence (PL) spectroscopy, shown in Figure S1. After which the samples were then reintroduced to the CVD chamber for the Sn treatment. In the second step, the as grown WS_2 layers were subsequently put under the Sn rich atmosphere via using the SnS as a precursor. It is noted that compared to the traditional method using tin dioxide (SnO_2) for the growth of tin-rich 2D materials, SnS precursor is advantageous for providing an environment with less oxygen contamination. The doping temperature were found to play a critical role in the control of substitution reaction of Sn, which will be discussed later.

Figure 1(b) schematically demonstrates the experimental setup for the synthesis of Sn doped WS_2 crystals using post thermal treatment method. The doping of Sn was carried out using a homebuilt 1-inch CVD system with quartz tube and gas flow rates controlled by digital mass flow controllers. Both the SnS precursor and the pre-grown WS_2 crystals were placed on the ceramic crucible, separated by around 7 cm with the SnS precursor being put in the center of the furnace. Figure 1(c) and (d) shows comparison of optical images for the as-grown triangular WS_2 before and after 10 min of the second Sn doping stage, demonstrating that there is no significant damage or change of morphology during the thermal doping process. Besides, both the WS_2 before and after Sn doping were further characterized by atomic force microscopy (AFM) which are shown in the Figure 1(e) and (f), respectively. After extracting from the dark yellow dashed line in Figure 1(e) and (f) across the step edge at the corner of WS_2 crystal, the line profiles (Figure 1(g)) reveal that the step height at the WS_2 edge are measured to be 0.77 nm before Sn doping and 0.81 nm after doping, respectively. This confirms that the thickness of WS_2 remains monolayer after the doping of Sn.

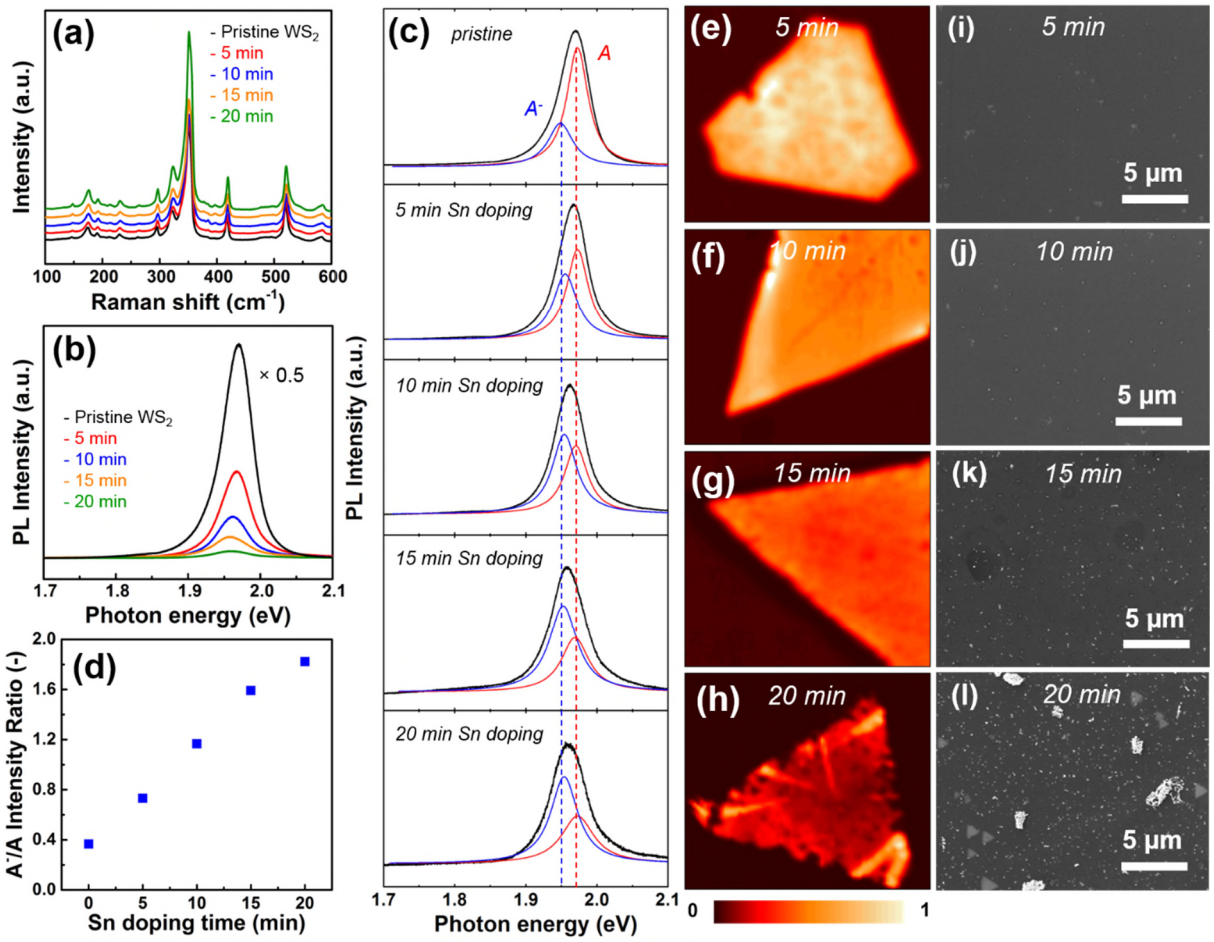

Figure 2. Characterization of Sn doped WS_2 with different Sn doping time. (a) Raman spectrum of monolayer WS_2 before and after 5, 10, 15, 20 min Sn doping. (b) PL spectrum of monolayer WS_2 before and after 5, 10, 15, 20 min Sn doping. (c) PL spectra of the pristine monolayer WS_2 and after each Sn doping time with the Lorentzian fitting by excitonic and trionic peaks. (d) Plot of intensity ratio between excitonic peak and trionic peak with the Sn doping time. (e-h) PL mapping of the WS_2 after (e) 5, (f) 10, (g) 15, (h) 20 min Sn doping, respectively. (i-l) SEM images of the surface of monolayer WS_2 after (i) 5, (j) 10, (k) 15, (l) 20 min Sn doping, respectively.

To further demonstrate the property change with the amount of Sn dopants, the Sn doped WS_2 crystals were synthesized with different Sn doping time and further characterized by spectroscopy. The Raman spectrum from Figure 2(a) demonstrates that there is no apparent peak shift between the pristine WS_2 and the WS_2 crystals after different Sn doping time (5, 10, 15, 20 min), indicating that the WS_2 monolayers remain high quality with little damage after

the doping of Sn. This is also evidenced by the comparison between Sn doped WS_2 monolayers with each Sn doping time and the corresponding pristine WS_2, demonstrated in Figure S2. In addition, only the two subtle peaks at 383 cm^{-1} and 397 cm^{-1} in the Raman spectrum are observed in the Sn doped WS_2 layers. These peaks are due to the Raman resonance effect resulted from the extrinsic substitutional dopants, which is also found in previous report.[51] The PL characteristic peak of WS_2, demonstrated in Figure 2(b), shows a gradual quenching with the increase of doping time and the concentration of Sn dopants. This indicates the increased free electron injection and the Sn dopants are functioned as electron donor (n-type dopants) when substituting the W atoms in the WS_2 layers.[52] Each PL spectrum was then deconvoluted into two separate peaks, corresponding to exciton (A) and trion (A^-) emission, using Lorentzian fitting shown in Figure 2(c). It can be seen that from Figure 2(d) the intensity ratio between extracted A^- and A peak rises with the increase of Sn doping time, indicating more negatively charged excitons resulted from the electron supply of extrinsic Sn atoms which is consistent with the PL quenching results. It is noted that the Ar annealing of monolayer WS_2 could also lead to the PL quenching due to the introduction of sulfur vacancies at high temperature; however, this effect could be minimized as the SnS precursor could provide additional sulfur during the Sn doping and potentially induce the self-healing of sulfur vacancies. The PL intensity of the resulted WS_2 with Sn doping is much smaller than that with Ar annealing under the same treatment time (Figure S3). This confirms that the PL quenching comes from the doping of Sn rather than the loss of sulfur atoms. Figure 2(e-h) shows the corresponding PL mapping of Sn doped WS_2 crystal with different Sn doping time. It can be seen that the PL intensities are relatively uniform over the entire Sn doped WS_2 layers except for the alloy after 20 min Sn doping, which may result from initiation of the WS_2 degradation as the supply of sulfur from SnS precursor becomes deficient to fill in the increasing sulfur vacancies. The SEM was employed to further examine the details on the change of WS_2 surfaces under different Sn

doping time. As shown in Figure 2(i-l), it can be seen that during the first 15 min of Sn doping, the WS_2 remains a clean surface, while after 20 min doping bunches of chunky white particles could be observed and the WS_2 starts to degrade and reveal triangular holes on the surfaces. For the further characterization of Sn doped WS_2 monolayers, we focused on the analysis of monolayer WS_2 after 10 min Sn doping and its comparison with the pristine monolayer WS_2 crystals.

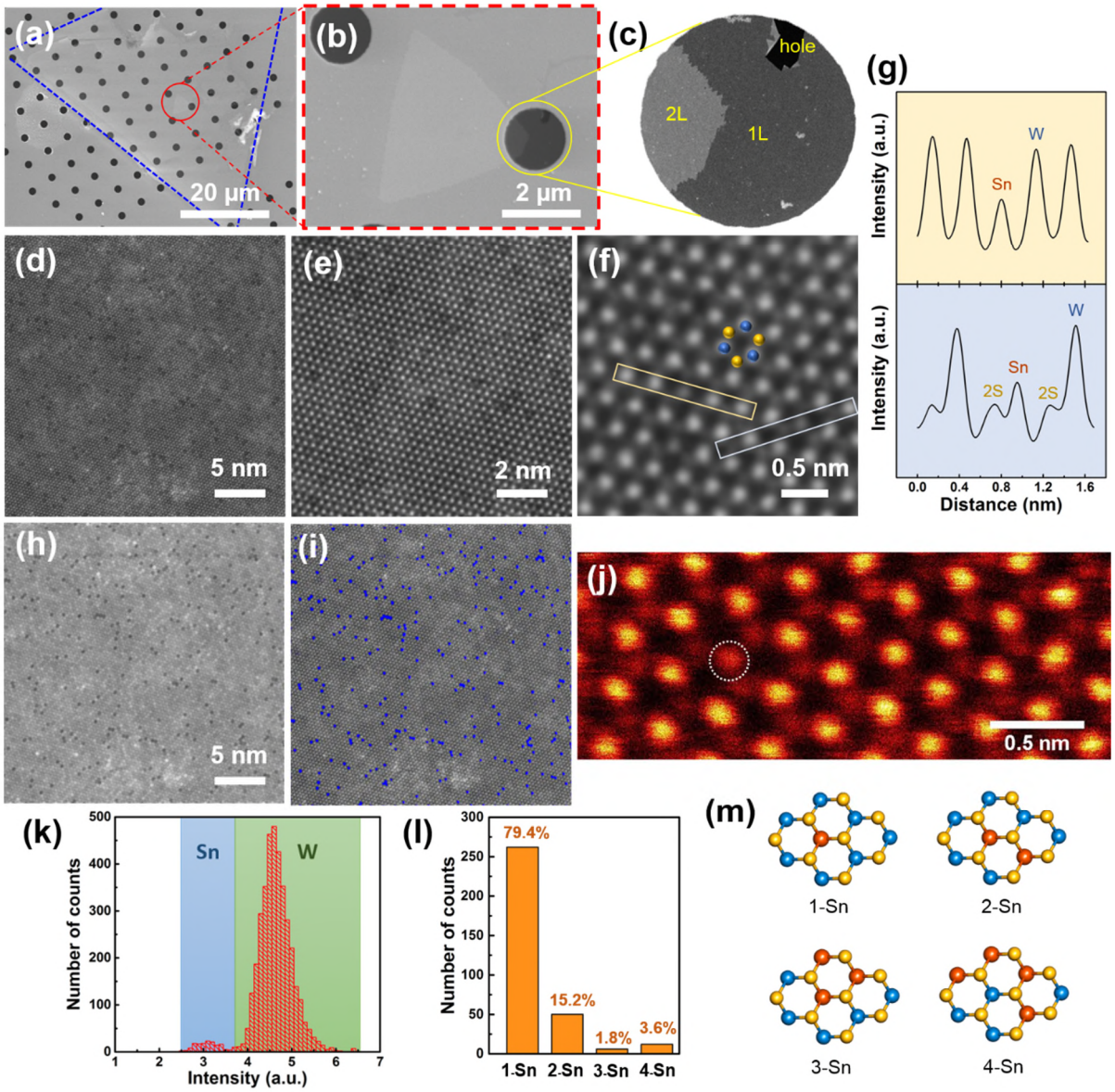

Figure 3. Annular dark field STEM (ADF-STEM) analysis of the monolayer Sn doped WS_2. (a) SEM image of Sn doped WS_2 transferred onto the SiN TEM grid. (b) Enlarged SEM image of red circle

indicated in (a) showing the details on the monolayer Sn doped WS_2 and a small island of bilayer Sn doped WS_2. (c) ADF-STEM image of the exact same area in (b). (d-f) ADF-STEM images showing the area of monolayer Sn doped WS_2 with different magnification. (g) Intensity line profiles across the yellow and blue rows in (f) showing the differences in intensity between W and Sn. (h) Maximum filter with the low magnification STEM image (d) displaying the distinct contrast between Sn dopant and W atoms. (i) Labeled-atom image obtained from (d) demonstrating the distribution of Sn dopant (blue dot). (j) High magnification ADF-STEM image of a Sn dopant in the WS_2 lattice with false color LUT (red-hot). White dashed circle indicates Sn site. (k) The histogram analysis of image (h) after applying the maximum filter. (l) The histogram analysis showing the percentage of different configurations of Sn dopants. (m) Atomic structure illustrations representing the four different configurations of Sn dopants that were observed in the labeled-atom image (h).

Although both SEM and PL studies provide useful insights for the characterization of the Sn doping of WS_2, they offer limited information for the quantification and distribution of Sn dopants in WS_2 monolayers. Direct imaging of Sn dopant using annular dark field scanning transmission electron microscope (ADF-STEM) is a powerful technique to further identify the location of Sn dopants within the WS_2. The SEM image in Figure 3(a) shows the triangular Sn doped WS_2 layers indicated by blue dashed lines transferred from SiO_2 substrate to a holy SiN grid after 10 min Sn doping for the characterization of ADF-STEM. The enlarged SEM image in Figure 3(b) demonstrates the details on center area of the triangular Sn doped WS_2 marked by red circle in Figure 3(a), showing the additional adlayer resulted from the overgrowth on monolayer WS_2 during the first step CVD synthesis process. To confirm the existence of Sn, the sample was firstly examined by EDX analysis shown in Figure S4(a). Figure 3(c) presents the ADF-STEM image of the yellow circle in Figure 3(b), displaying a clear boundary between the monolayer and bilayer doped WS_2. Figure 3(d-f) demonstrates typical ADF-STEM images with different magnification of the Sn doped WS_2.

In ADF-STEM imaging, the primary contrast mechanism is Z-contrast. The collected signal in the ADF-STEM images is directly proportional to $Z^{1.6}$, meaning the elements with higher atomic numbers (higher Z) exhibit higher intensity in the image. This enables atoms of different elements to be discriminated on the basis of their contrast difference. After introducing the optical aberration system, the imaging technique is capable of identifying and locating different elements. In the Sn doped WS_2 crystals, W atoms (Z=74) appear with higher intensity than double S (Z=16) columns and the Sn (Z=50) atom can also be distinguished from double S columns and single W column. From the line intensity scan (Figure 3(g)) extracted in the blue and yellow column in Figure 3(f), it is clearly observed that the Sn atoms are all situated at the W sites, suggesting the substitutional doping of Sn with the W in the WS_2. To confirm that the dimmer spot is Sn atom, the experimental intensity line profile was also compared with the simulated Z-contrast intensity profile and shows a great match with the Sn simulation result (Figure S4(b)) rather than other metal dopant such as Cr which could be possibly from the trace elements of the metal oxide precursors.[53] A higher magnification ADF-STEM image is shown in Figure 3(j) in false color to show the Sn dopant locations (white circles). Besides, the sulfur maintain stacking vertically together based on the line scan along the $[11\bar{2}0]$ direction (blue column in Figure 3(f)), suggesting the whole alloy structure remains 2H phase after the doping of Sn. To further determine the composition of the Sn doped WS_2 sample, a maximum filter (Figure 3(h)) was firstly applied on the low magnification ADF-STEM image of Figure 3(d) to reveal the contrast difference between Sn and W. Statistical counting of individual W/Sn site in the Figure 3(h) was then adopted and the histogram of intensity of each site is shown in Figure 3(l). Through applying an approximate threshold at the intensity of 3.8 arbitrary unit (a.u.), the original image with the Sn dopants highlighted by blue dot could be obtained (Figure 3(i)) and the atomic percentage of the Sn in Sn doped WS_2 monolayer can be estimated around 8.16%. In addition, it can be seen that the arrangement of

Sn dopants in $Sn_xW_{(1-x)}S_2$ alloy differs from mono-Sn (1-Sn), bi-Sn (2-Sn), tri-Sn (3-Sn) to tetra-Sn (4-Sn) dopants, where the atomic structures are illustrated in Figure 3(l). The statistical distribution in Figure 3(k) shows that among the Sn dopants, around 80% of them are arranged in 1-Sn. This indicates the little preference for the Sn dopants to cluster in the WS_2 layers and the doping of Sn is fairly uniform.

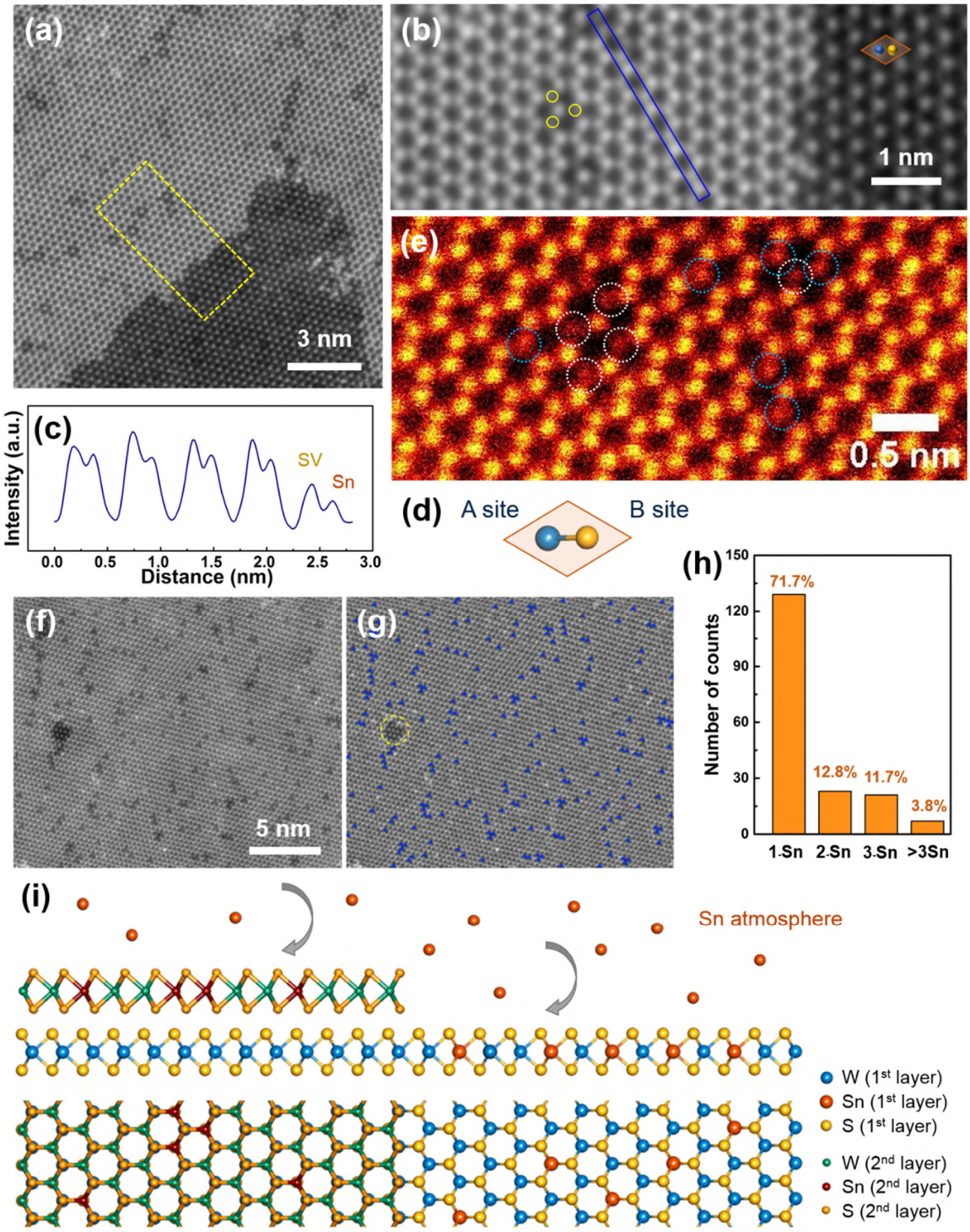

Figure 4. ADF-STEM analysis of the bilayer Sn doped WS_2. (a) Low magnification ADF-STEM image showing the boundary between the monolayer and bilayer Sn doped WS_2. (b) Enlarged ADF-STEM image from the yellow dashed square in (a). (c) Intensity line profile across the blue row in (b) showing the differences in intensity between W and Sn sites and sulfur vacancies in the bilayer regions. (d) Schematic illustration of a unit cell extracted from (b) with a metal atom situated on A site and two

chalcogen atoms on B site. (e) High magnification ADF-STEM image of Sn dopants in bilayer WS_2. White dashed circles indicate Sn dopants and blue dashed circles indicate S vacancy sites. (f) Low magnification ADF-STEM image of bilayer Sn doped WS_2. (g) Labeled-atom image obtained from (f) demonstrating the distribution of Sn dopant (blue dot). (h) The histogram analysis from (g) showing the percentage of different configurations of Sn dopants. (i) Atomic structure illustrations for both the top and side views of the Sn doped WS_2 showing the tin dopants are only introduced at the top layer of WS_2.

To further understand the Sn doping we examined the monolayer-bilayer step edge region of Sn doped WS_2, as shown in Figure 3(b), using ADF-STEM. This enables the relative orientation of the two layers to be known and the sub-lattice sites. Figure 4(a) illustrates a low magnification of ADF-STEM image at the monolayer-bilayer interface. Figure 4(b) is the further magnified ADF-STEM image of the yellow dashed square in Figure 4(a), demonstrating the intensity details on each lattice site. It can be seen that the bilayer Sn doped WS_2 follows the 2H stacking sequence, where the single W/Sn (double S) column in one layer overlaps with the double S (single W/Sn) column in the other layer. The two layers are fully eclipsed with a rotation angle of 60° between each lattice orientation. Figure 4(c) shows the intensity profile of the line scan along the $[11\bar{2}0]$ direction indicated by blue column in Figure 4(b). The lattice sites with the largest intensity are corresponded to the superimposition of one W atom and two S atoms. The two lattice sites with lower intensity in Figure 4(c) are corresponded to the Sn dopants and sulfur vacancy (SV), respectively. It is noted that the Sn dopants in the bilayer Sn doped WS_2 are slightly dimmer than the SV due to the smaller Z in total. On the basis of these intensity difference, the Sn dopant sites could be distinguished, which enables the analysis of dopant distribution in the bilayer Sn doped WS_2. A higher magnification ADF-STEM image of the bilayer region is shown in Figure 4(e) in false color to show the Sn dopant locations (white circles) and S vacancy sites (blue circles).

To further locate the Sn dopant site in each layer, a rhombohedral unit cell illustrated in Figure 4(d) containing one W atom located at the A site and two overlapped S atoms situated at the B sites was extracted from Figure 4(b). Due to the 2H stacking sequence, it is inferred that on the second layer of Sn doped WS_2, the W and S atoms swap with each other with S atoms at the A site and the W atom at the B site. After careful examination, it is found that all the Sn dopants are situated at the B sites rather than A sites in bilayer Sn doped WS_2. This indicates that the Sn dopants are only introduced in the secondary layer rather than bottom layer in the bilayer Sn doped WS_2 where the atomic configuration are demonstrated in Figure 4(i). This selective doping from only top surface could potentially establish a vertical heterojunction in bilayer crystals, which has not been reported in previous studies. Figure 4(f) shows the low magnification of the bilayer Sn doped WS_2. Using the similar technique by setting the threshold intensity, each Sn dopant in the bilayer region could be located. The yellow dashed circle in the Figure 4(g) reveals the contrast of monolayer Sn doped WS_2, which could probably stem from the electron beam damage. After counting each Sn dopants in the bilayer region, the statistical distribution in the Figure 4(h) shows that the 1-Sn remains dominant arrangement, around 70% among all the Sn dopants.

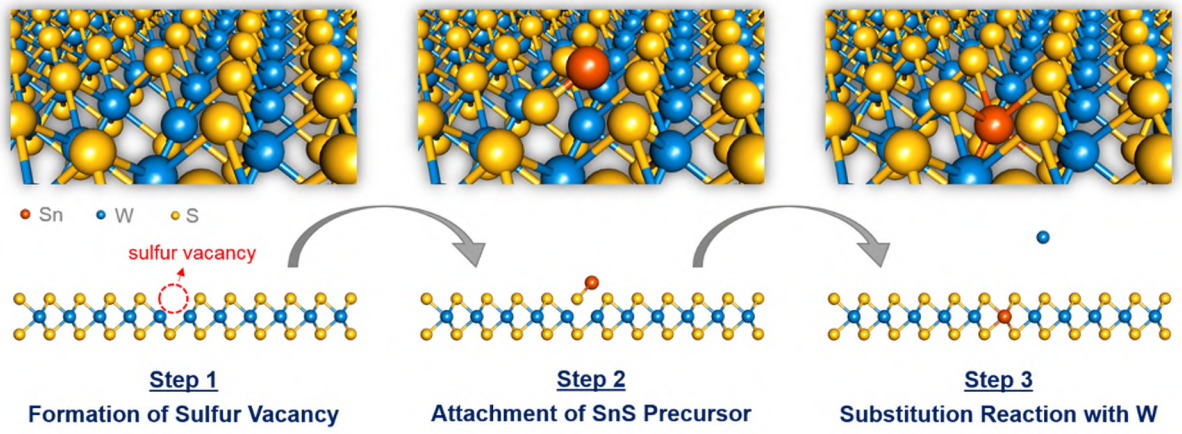

Figure 5. Doping mechanism of Sn substituting into W site in the WS_2 layers.

In addition, the doping temperature is found to be critical in controlling the substitution reaction in the WS_2 layers. As shown in Figure S5, when decreasing the doping temperature to 450°C, a high density of the Sn dopants are distributed nearby the domain boundaries rather than the entire WS_2 layers. This could be ascribed to the substitution reaction driven by the sulfur vacancies during the doping process. As shown in Figure 5, during the thermal doping process the presence of sulfur vacancy could lower the structural stability of WS_2 layer (Step 1) and the SnS precursors are likely to be firstly incorporated on the active sites nearby the sulfur vacancies (Step 2). After which the SnS tend to substitute the nearest unsaturated W sites, this includes the dissociation of neighboring five W-S bonding, the formation of new five Sn-S bonding and additional two W-S bonding associated with the original sulfur vacancies (Step 3). The bonding energy for W-S and Sn-S are reported to be 648 kJ/mol and 464 kJ/mol, respectively.[54-55] The enthalpy of the Sn substitution reaction is therefore estimate to be -376 kJ/mol, indicating a more energetically favorable and stable structure of Sn doped WS_2. Because the sulfur vacancies also help to lower the formation energy of domain boundaries in WS_2 and could promote the formation of domain boundary, which are composed of several pentagon-heptagon pairs with unsaturated bonding.[56] When the doping temperature decreases to 450°C, the thermally induced sulfur vacancies are greatly reduced and most of the remaining

sulfur vacancies primarily comes from the area nearby the domain boundaries. As a consequence, the Sn doping is greatly suppressed at the lower doping temperature and could only introduce to the imperfection sites that are easier for the creation of sulfur vacancies.

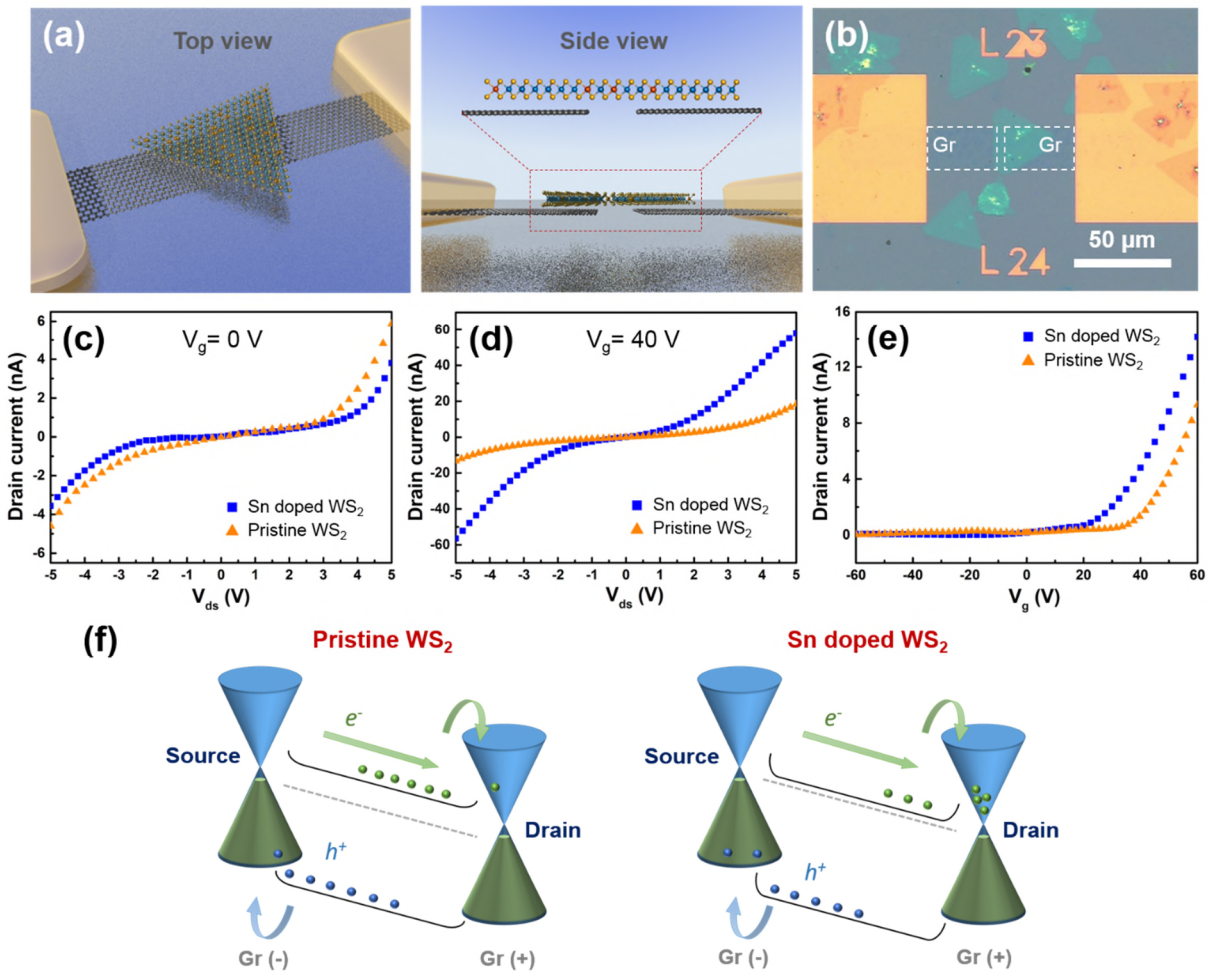

Figure 6. Electrical measurement of pristine and Sn doped WS_2 layers. (a) Schematic illustrations of device based on monolayer Sn doped WS_2 connected to patterned Gr ribbons. (b) Optical image of the fabricated device with Sn doped WS_2 monolayer bridged by graphene ribbons. (c) Output characteristics of the pristine and Sn doped WS_2 monolayers without applying the gate voltage. (d) Output characteristics of the pristine and Sn doped WS_2 monolayers under the gate voltage of 40 V. (e) Transfer characteristic curves of the bottom-gate devices based on pristine and Sn doped WS_2 monolayers under the bias of 2 V. (f) Energy band diagram for the pristine WS_2 and Sn doped WS_2 monolayer at the Gr contacts.

For the purpose of characterizing the electrical properties, we then fabricated the bottom-gated transistors both with the pristine WS_2 and Sn doped WS_2 layers, which have the channel length of 1 μm and channel width of 25 μm; the details on device fabrication is described in the Methods sections. Figure 6(a) schematically shows the top view and side view of the as-fabricated device, which comprises gapped graphene ribbons with the Sn doped WS_2 crystal in the middle. Figure 6(b) shows the optical image of the device, the gap between graphene ribbons is 1 μm and both the ribbons are connected to Cr/Au (10 nm/80 nm) bond pads individually. To compare the doping effect on the electrical properties, both the pristine and Sn doped WS_2 layers are transferred on top of the gap between graphene ribbons individually. The IV measurement in Figure 6(c) shows that the monolayer Sn doped WS_2 exhibits a lower current signal comparing to the pristine WS_2, which could possibly be attributed to the damaging of WS_2 layer during the Sn substitution reaction. The nonlinear curves indicates the Schottky contact at the interface between both the WS_2 layers and graphene ribbons. When applying the gate voltage of 40 V, the current signal of Sn doped WS_2 layer becomes four times larger than that of pristine WS_2 shown in Figure 6(d). Besides, both the I-V characteristics of pristine WS_2 and Sn doped WS_2 are more linear compared to those measured without gate bias, indicating the reducing Schottky barrier height at the graphene-WS_2 contacts. The transfer characteristic curves of pristine WS_2 and Sn doped WS_2 monolayers are demonstrated in Figure 6(e), both of which shows a typical behavior of n-type semiconductor. Besides, it is observed that the doping of Sn significantly affects the threshold voltage (V_{th}), which could be obtained from the extrapolation in the linear region of the transfer characteristic curves, towards the neutral point. For the device based on pristine WS_2 monolayers, the V_{th} is found to be around 35 V which is consistent to our previous report,[9,48] whereas in the device with Sn doped WS_2 monolayers the V_{th} has a negative shift to 22 V. This indicates the n-type doping resulted from the Sn substitution, which is consistent with the PL

quenching phenomenon. The energy band diagrams in Figure 6(f) further explain that the n-type doping of Sn makes the Fermi level approach closer to the conduction band of WS_2, resulting in the smaller gate voltage to reach its ON-state and the negative shift of transfer curve. The carrier injection within Sn doped WS_2 to the external circuit is therefore more efficient under the positive gate.

Conclusion

In summary, we have demonstrated the post-growth modification by metallic Sn substitution in the monolayer and bilayer WS_2 crystals grown by CVD. This method separates the growth stage of host 2D materials and thermal doping stage of extrinsic atoms, which has a better control of dopants spatial distribution. The substitution relies on the sulfur vacancies and the bonding between W and Sn, it is therefore more favorable under high doping temperature. In bilayer WS_2 crystals, the Sn substitutional doping only introduces from the top layer resulting in a selective layer doping and potentially creating vertical heterostructures. The electrical measurement of transfer characteristics indicates the n-type doping of WS_2 layers after the Sn substitution, which is consistent with the PL quenching phenomenon. These results provide a new route of structural modification for 2D materials and pave the way for the adjustment of components in 2D materials that meet various application requirements.

Methods

Post-growth Sn doping of WS_2 layers

The single-crystalline monolayer WS_2 was firstly synthesized by atmospheric chemical vapor deposition using sulfur and tungsten trioxide as precursors and followed by the second step of Sn thermal doping. During the Sn doping stage, 3 mg of SnS was loaded at the center of the furnace and the as-grown WS_2 was placed in the downstream of furnace in the 1 inch

quartz tube, about 5 cm away from the SnS. The Sn thermal doping of WS_2 was conducted at the atmospheric condition. After loading the precursors and monolayer WS_2, the whole system was flushed with 500 sccm Ar gas for 30 min to remove the residual air. The temperature in the furnace was then raised to 550 °C in 30 min with 100 sccm Ar flow and maintained for some time (5-20 min) to conduct the doping of Sn before cooled down to room temperature.

Transfer of Sn doped WS_2 layers

After completion of the synthesis, the Sn doped WS_2 layers on the SiO_2/Si was first spin-coated with a supporting polymer film, polymethylmethacrylate (PMMA), at 4500 rpm for 60 s. The substrate was then floated on 1 M aqueous potassium hydroxide solution to etch the SiO_2. After the SiO_2 had been s removed by the etchant solution, the PMMA/ Sn doped WS_2 stack was then rinsed by transferring on deionized water three times to eliminate the residual ions from the etchant solution. The rinsed stack was subsequently transferred onto a holey silicon nitride grid and dried in air overnight, followed by baking at 180 °C for 30 min to enhance the adhesion at the interface of the grid and Sn doped WS_2 layers. Finally, the PMMA supporting layer was removed by submerging the sample in acetone for 12 h.

STEM characterization for the substitution doping of Sn

ADF-STEM imaging was performed using a JEOL ARM200F at 80 kV located at the David Cockayne Centre for Electron Microscopy (DCCEM). Imaging conditions used were a 30 μm CL aperture with a convergence semiangle of 22.5 mrad and a beam current of 35 pA. The acquisition angles for these images were 73–271 mrad.

Characterization of Sn doped WS_2 layers

Scanning electron microscopy (SEM) was performed using a Hitachi-4300 FEG with an accelerating voltage of 3.0 kV. Raman spectroscopy was carried out using a JY Horiba

LabRAM Aramis imaging confocal Raman microscope under an excitation wavelength of 532 nm at 12.5mW power focused to a 1 μm spot size. Atomic force microscopy (AFM) was performed using an Asylum Research MFP-3D in AC mode with a silicon AC-160TS cantilever (Olympus, spring constant ~42 N/m and resonant frequency ~300 kHz). Measurements were all done in room-temperature under ambient pressure.

Device fabrication

JEOL 5500 FS EBL system was used to write the designed patterns of bond pads in a bilayer PMMA (A8 495k and A8 950k) resist. A thermal evaporator was used to deposit Cr/Au (10 nm/80 nm) bond pads onto s 300 nm SiO_2/Si substrate, followed by liftoff in hot acetone. PMMA/graphene film was transferred onto the Si chip with prepatterned bond pads, and baked overnight at 180°C for better contact. Graphene film was then patterned using EBL with negative resist (ma-N 2403) and reactive ion etching (RIE) etching to define graphene channels with a length and width of 100 and 25 μm, respectively. The 1 μm gaps between graphene channels were fabricated using the same process. Lastly, the PMMA/WS_2 film was transferred to the sample.

Electrical characterization of Sn doped WS_2 devices

A Keithley 2400 source meter was used for the measurement of I-V characteristics and gate dependent transistor measurements of both the pristine and Sn doped WS_2. Highly conductive Si in the substrate was wired and connected to a socket as a back gate. Tungsten tips connected to a Keithley 2400 source meter are used to probe the metal bond-pads of each devices and to apply a bias sweep from -5 V to + 5 V. Measurements were all done in room-temperature under ambient pressure.

Associated content

Supporting information

Atmospheric pressure chemical vapor deposition (CVD) synthesis of WS_2 domains on the SiO_2 substrate, morphology comparison of WS_2 before and after Sn doping, comparison of PL characterization peak intensity between the pristine monolayer WS_2, pristine WS_2 after 10 min Ar annealing and Sn doped WS_2 monolayer obtained from 10 min Sn doping of WS_2, element analysis for the confirmation of Sn dopants in WS_2 layers, ADF-STEM analysis of Sn doped WS_2 domain boundaries obtained under the low Sn doping temperature.

Author information

Corresponding author

*E-mail: jamie.warner@materials.ox.ac.uk.

Acknowledgements

J.H.W. thanks the Royal Society and the European Research Council for support. R.C. acknowledges the support from Taiwan Government Scholarship to Study Abroad.

Reference

(1) Novoselov, K. S.; Geim, A. K.; Morozov, S. V.; Jiang, D.; Zhang, Y.; Dubonos, S. V.; Grigorieva, I. V.; Firsov, A. A., Electric Field Effect in Atomically Thin Carbon Films. *Science* **2004,** *306* (5696), 666-669.

(2) Novoselov, K. S.; Jiang, D.; Schedin, F.; Booth, T. J.; Khotkevich, V. V.; Morozov, S. V.; Geim, A. K., Two-Dimensional Atomic Crystals. *Proc. Natl. Acad. Sci. U.S.A.* **2005,** *102* (30), 10451-10453.

(3) Manzeli, S.; Ovchinnikov, D.; Pasquier, D.; Yazyev, O. V.; Kis, A., 2D Transition Metal Dichalcogenides. *Nat. Rev. Mater.* **2017,** *2*, 17033.

(4) Splendiani, A.; Sun, L.; Zhang, Y.; Li, T.; Kim, J.; Chim, C.-Y.; Galli, G.; Wang, F., Emerging Photoluminescence in Monolayer MoS_2. *Nano Lett.* **2010,** *10* (4), 1271-1275.

(5) Ganatra, R.; Zhang, Q., Few-Layer MoS_2: A Promising Layered Semiconductor. *ACS Nano* **2014,** *8* (5), 4074-4099.

(6) Furchi, M. M.; Polyushkin, D. K.; Pospischil, A.; Mueller, T., Mechanisms of Photoconductivity in Atomically Thin MoS_2. *Nano Lett.* **2014,** *14* (11), 6165-6170.

(7) Buscema, M.; Island, J. O.; Groenendijk, D. J.; Blanter, S. I.; Steele, G. A.; van der Zant, H. S. J.; Castellanos-Gomez, A., Photocurrent Generation with Two-Dimensional van der Waals Semiconductors. *Chem. Soc. Rev.* **2015,** *44* (11), 3691-3718.

(8) Tan, H.; Fan, Y.; Zhou, Y.; Chen, Q.; Xu, W.; Warner, J. H., Ultrathin 2D Photodetectors Utilizing Chemical Vapor Deposition Grown WS_2 With Graphene Electrodes. *ACS Nano* **2016,** *10* (8), 7866-7873.

(9) Tan, H.; Xu, W.; Sheng, Y.; Lau, C. S.; Fan, Y.; Chen, Q.; Tweedie, M.; Wang, X.; Zhou, Y.; Warner, J. H., Lateral Graphene-Contacted Vertically Stacked WS_2/MoS_2 Hybrid Photodetectors with Large Gain. *Adv. Mater.* **2017,** *29* (46), 1702917.

(10) Wang, H.; Yu, L.; Lee, Y.-H.; Shi, Y.; Hsu, A.; Chin, M. L.; Li, L.-J.; Dubey, M.; Kong, J.; Palacios, T., Integrated Circuits Based on Bilayer MoS_2 Transistors. *Nano Lett.* **2012,** *12* (9), 4674-4680.

(11) Roy, T.; Tosun, M.; Kang, J. S.; Sachid, A. B.; Desai, S. B.; Hettick, M.; Hu, C. C.; Javey, A., Field-Effect Transistors Built from All Two-Dimensional Material Components. *ACS Nano* **2014,** *8* (6), 6259-6264.

(12) Withers, F.; Del Pozo-Zamudio, O.; Mishchenko, A.; Rooney, A. P.; Gholinia, A.; Watanabe, K.; Taniguchi, T.; Haigh, S. J.; Geim, A. K.; Tartakovskii, A. I.; Novoselov, K. S., Light-Emitting Diodes by Band-Structure Engineering in van der Waals

Heterostructures. *Nat. Mater.* **2015,** *14* (3), 301-306.

(13) Jariwala, D.; Davoyan, A. R.; Wong, J.; Atwater, H. A., Van der Waals Materials for Atomically-Thin Photovoltaics: Promise and Outlook. *ACS Photonics* **2017,** *4* (12), 2962-2970.

(14) Xu, X.; Yao, W.; Xiao, D.; Heinz, T. F., Spin and Pseudospins in Layered Transition Metal Dichalcogenides. *Nat. Phys.* **2014,** *10*, 343-350.

(15) Ning, C.-Z.; Dou, L.; Yang, P., Bandgap Engineering in Semiconductor Alloy Nanomaterials with Widely Tunable Compositions. *Nat. Rev. Mater.* **2017,** *2*, 17070.

(16) Pham, V. P.; Yeom, G. Y., Recent Advances in Doping of Molybdenum Disulfide: Industrial Applications and Future Prospects. *Adv. Mater.* **2016,** *28* (41), 9024-9059.

(17) Cheng, Y. C.; Zhu, Z. Y.; Mi, W. B.; Guo, Z. B.; Schwingenschlögl, U., Prediction of Two-Dimensional Diluted Magnetic Semiconductors: Doped Monolayer MoS_2 Systems. *Phys. Rev. B* **2013,** *87* (10), 100401.

(18) Zhang, K.; Feng, S.; Wang, J.; Azcatl, A.; Lu, N.; Addou, R.; Wang, N.; Zhou, C.; Lerach, J.; Bojan, V.; Kim, M. J.; Chen, L.-Q.; Wallace, R. M.; Terrones, M.; Zhu, J.; Robinson, J. A., Manganese Doping of Monolayer MoS_2: The Substrate Is Critical. *Nano Lett.* **2015,** *15* (10), 6586-6591.

(19) Li, B.; Xing, T.; Zhong, M.; Huang, L.; Lei, N.; Zhang, J.; Li, J.; Wei, Z., A Two-Dimensional Fe-Doped SnS_2 Magnetic Semiconductor. *Nat. Commun.* **2017,** *8* (1), 1958.

(20) Suh, J.; Park, T.-E.; Lin, D.-Y.; Fu, D.; Park, J.; Jung, H. J.; Chen, Y.; Ko, C.; Jang, C.; Sun, Y.; Sinclair, R.; Chang, J.; Tongay, S.; Wu, J., Doping against the Native Propensity of MoS_2: Degenerate Hole Doping by Cation Substitution. *Nano Lett.* **2014,** *14* (12), 6976-6982.

(21) Zhang, K.; Bersch, B. M.; Joshi, J.; Addou, R.; Cormier, C. R.; Zhang, C.; Xu, K.; Briggs, N. C.; Wang, K.; Subramanian, S.; Cho, K.; Fullerton-Shirey, S.; Wallace, R. M.; Vora, P. M.; Robinson, J. A., Tuning the Electronic and Photonic Properties of Monolayer MoS_2 via in Situ Rhenium Substitutional Doping. *Adv. Funct. Mater.* **2018,** *28* (16), 1706950.

(22) Chen, Y.; Xi, J.; Dumcenco, D. O.; Liu, Z.; Suenaga, K.; Wang, D.; Shuai, Z.; Huang, Y.-S.; Xie, L., Tunable Band Gap Photoluminescence from Atomically Thin Transition-Metal Dichalcogenide Alloys. *ACS Nano* **2013,** *7* (5), 4610-4616.

(23) Liu, X.; Wu, J.; Yu, W.; Chen, L.; Huang, Z.; Jiang, H.; He, J.; Liu, Q.; Lu, Y.; Zhu, D.; Liu, W.; Cao, P.; Han, S.; Xiong, X.; Xu, W.; Ao, J.-P.; Ang, K.-W.; He, Z.,

Monolayer $W_xMo_{1-x}S_2$ Grown by Atmospheric Pressure Chemical Vapor Deposition: Bandgap Engineering and Field Effect Transistors. *Adv. Funct. Mater.* **2017,** *27* (13), 1606469.

(24) Zhang, M.; Wu, J.; Zhu, Y.; Dumcenco, D. O.; Hong, J.; Mao, N.; Deng, S.; Chen, Y.; Yang, Y.; Jin, C.; Chaki, S. H.; Huang, Y.-S.; Zhang, J.; Xie, L., Two-Dimensional Molybdenum Tungsten Diselenide Alloys: Photoluminescence, Raman Scattering, and Electrical Transport. *ACS Nano* **2014,** *8* (7), 7130-7137.

(25) Li, H.; Duan, X.; Wu, X.; Zhuang, X.; Zhou, H.; Zhang, Q.; Zhu, X.; Hu, W.; Ren, P.; Guo, P.; Ma, L.; Fan, X.; Wang, X.; Xu, J.; Pan, A.; Duan, X., Growth of Alloy $MoS_{2x}Se_{2(1-x)}$ Nanosheets with Fully Tunable Chemical Compositions and Optical Properties. *J. Am. Chem. Soc.* **2014,** *136* (10), 3756-3759.

(26) Li, H.; Zhang, Q.; Duan, X.; Wu, X.; Fan, X.; Zhu, X.; Zhuang, X.; Hu, W.; Zhou, H.; Pan, A.; Duan, X., Lateral Growth of Composition Graded Atomic Layer $MoS_{2(1-x)}Se_{2x}$ Nanosheets. *J. Am. Chem. Soc.* **2015,** *137* (16), 5284-5287.

(27) Duan, X.; Wang, C.; Fan, Z.; Hao, G.; Kou, L.; Halim, U.; Li, H.; Wu, X.; Wang, Y.; Jiang, J.; Pan, A.; Huang, Y.; Yu, R.; Duan, X., Synthesis of $WS_{2x}Se_{2-2x}$ Alloy Nanosheets with Composition-Tunable Electronic Properties. *Nano Lett.* **2016,** *16* (1), 264-269.

(28) Wu, X.; Li, H.; Liu, H.; Zhuang, X.; Wang, X.; Fan, X.; Duan, X.; Zhu, X.; Zhang, Q.; Meixner, A. J.; Duan, X.; Pan, A., Spatially Composition-Modulated Two-Dimensional $WS_{2x}Se_{2(1-x)}$ Nanosheets. *Nanoscale* **2017**, *9* (14), 4707-4712.

(29) Wang, Y.; Le, H.; Li, B.; Shang, J.; Xia, C.; Fan, C.; Deng, H.-X.; Wei, Z.; Li, J., Composition-Tunable 2D $SnSe_{2(1-x)}S_{2x}$ Alloys towards Efficient Bandgap Engineering and High Performance (Opto)Electronics. *J. Mater. Chem. C* **2017,** *5* (1), 84-90.

(30) Cui, F.; Feng, Q.; Hong, J.; Wang, R.; Bai, Y.; Li, X.; Liu, D.; Zhou, Y.; Liang, X.; He, X.; Zhang, Z.; Liu, S.; Lei, Z.; Liu, Z.; Zhai, T.; Xu, H., Synthesis of Large-Size 1T′ $ReS_{2x}Se_{2(1-x)}$ Alloy Monolayer with Tunable Bandgap and Carrier Type. *Adv. Mater.* **2017,** *29* (46), 1705015.

(31) Wang, Z.; Liu, P.; Ito, Y.; Ning, S.; Tan, Y.; Fujita, T.; Hirata, A.; Chen, M., Chemical Vapor Deposition of Monolayer $Mo_{1-x}W_xS_2$ Crystals with Tunable Band Gaps. *Sci. Rep.* **2016,** *6*, 21536.

(32) Yang, S.-Z.; Gong, Y.; Manchanda, P.; Zhang, Y.-Y.; Ye, G.; Chen, S.; Song, L.; Pantelides, S. T.; Ajayan, P. M.; Chisholm, M. F.; Zhou, W., Rhenium-Doped and Stabilized MoS_2 Atomic Layers with Basal-Plane Catalytic Activity. *Adv. Mater.* **2018,**

30 (51), 1803477.

(33) Rhodes, D.; Chenet, D. A.; Janicek, B. E.; Nyby, C.; Lin, Y.; Jin, W.; Edelberg, D.; Mannebach, E.; Finney, N.; Antony, A.; Schiros, T.; Klarr, T.; Mazzoni, A.; Chin, M.; Chiu, Y. c.; Zheng, W.; Zhang, Q. R.; Ernst, F.; Dadap, J. I.; Tong, X.; Ma, J.; Lou, R.; Wang, S.; Qian, T.; Ding, H.; Osgood, R. M.; Paley, D. W.; Lindenberg, A. M.; Huang, P. Y.; Pasupathy, A. N.; Dubey, M.; Hone, J.; Balicas, L., Engineering the Structural and Electronic Phases of $MoTe_2$ through W Substitution. *Nano Lett.* **2017,** *17* (3), 1616-1622.

(34) Kiriya, D.; Tosun, M.; Zhao, P.; Kang, J. S.; Javey, A., Air-Stable Surface Charge Transfer Doping of MoS_2 by Benzyl Viologen. *J. Am. Chem. Soc.* **2014,** *136* (22), 7853-7856.

(35) Choi, M. S.; Qu, D.; Lee, D.; Liu, X.; Watanabe, K.; Taniguchi, T.; Yoo, W. J., Lateral MoS_2 p–n Junction Formed by Chemical Doping for Use in High-Performance Optoelectronics. *ACS Nano* **2014,** *8* (9), 9332-9340.

(36) Gong, Y.; Yuan, H.; Wu, C.-L.; Tang, P.; Yang, S.-Z.; Yang, A.; Li, G.; Liu, B.; van de Groep, J.; Brongersma, M. L.; Chisholm, M. F.; Zhang, S.-C.; Zhou, W.; Cui, Y., Spatially Controlled Doping of Two-Dimensional SnS_2 Through Intercalation for Electronics. *Nat. Nanotechnol.* **2018,** *13*, 294-299.

(37) Gong, Y.; Liu, Z.; Lupini, A. R.; Shi, G.; Lin, J.; Najmaei, S.; Lin, Z.; Elías, A. L.; Berkdemir, A.; You, G.; Terrones, H.; Terrones, M.; Vajtai, R.; Pantelides, S. T.; Pennycook, S. J.; Lou, J.; Zhou, W.; Ajayan, P. M., Band Gap Engineering and Layer-by-Layer Mapping of Selenium-Doped Molybdenum Disulfide. *Nano Lett.* **2014,** *14* (2), 442-449.

(38) Gao, J.; Kim, Y. D.; Liang, L.; Idrobo, J. C.; Chow, P.; Tan, J.; Li, B.; Li, L.; Sumpter, B. G.; Lu, T.-M.; Meunier, V.; Hone, J.; Koratkar, N., Transition-Metal Substitution Doping in Synthetic Atomically Thin Semiconductors. *Adv. Mater.* **2016,** *28* (44), 9735-9743.

(39) Susarla, S.; Kochat, V.; Kutana, A.; Hachtel, J. A.; Idrobo, J. C.; Vajtai, R.; Yakobson, B. I.; Tiwary, C. S.; Ajayan, P. M., Phase Segregation Behavior of Two-Dimensional Transition Metal Dichalcogenide Binary Alloys Induced by Dissimilar Substitution. *Chem. Mater.* **2017,** *29* (17), 7431-7439.

(40) Kochat, V.; Apte, A.; Hachtel, J. A.; Kumazoe, H.; Krishnamoorthy, A.; Susarla, S.; Idrobo, J. C.; Shimojo, F.; Vashishta, P.; Kalia, R.; Nakano, A.; Tiwary, C. S.; Ajayan, P. M., Re Doping in 2D Transition Metal Dichalcogenides as a New Route to Tailor

Structural Phases and Induced Magnetism. *Adv. Mater.* **2017,** *29* (43), 1703754.

(41) Susarla, S.; Kutana, A.; Hachtel, J. A.; Kochat, V.; Apte, A.; Vajtai, R.; Idrobo, J. C.; Yakobson, B. I.; Tiwary, C. S.; Ajayan, P. M., Quaternary 2D Transition Metal Dichalcogenides (TMDs) with Tunable Bandgap. *Adv. Mater.* **2017,** *29* (35), 1702457.

(42) Yang, L.; Majumdar, K.; Liu, H.; Du, Y.; Wu, H.; Hatzistergos, M.; Hung, P. Y.; Tieckelmann, R.; Tsai, W.; Hobbs, C.; Ye, P. D., Chloride Molecular Doping Technique on 2D Materials: WS_2 and MoS_2. *Nano Lett.* **2014,** *14* (11), 6275-6280.

(43) Azcatl, A.; Qin, X.; Prakash, A.; Zhang, C.; Cheng, L.; Wang, Q.; Lu, N.; Kim, M. J.; Kim, J.; Cho, K.; Addou, R.; Hinkle, C. L.; Appenzeller, J.; Wallace, R. M., Covalent Nitrogen Doping and Compressive Strain in MoS_2 by Remote N_2 Plasma Exposure. *Nano Lett.* **2016,** *16* (9), 5437-5443.

(44) Nipane, A.; Karmakar, D.; Kaushik, N.; Karande, S.; Lodha, S., Few-Layer MoS_2 p-Type Devices Enabled by Selective Doping Using Low Energy Phosphorus Implantation. *ACS Nano* **2016,** *10* (2), 2128-2137.

(45) Li, H.; Wu, X.; Liu, H.; Zheng, B.; Zhang, Q.; Zhu, X.; Wei, Z.; Zhuang, X.; Zhou, H.; Tang, W.; Duan, X.; Pan, A., Composition-Modulated Two-Dimensional Semiconductor Lateral Heterostructures via Layer-Selected Atomic Substitution. *ACS Nano* **2017,** *11* (1), 961-967.

(46) Lu, A.-Y.; Zhu, H.; Xiao, J.; Chuu, C.-P.; Han, Y.; Chiu, M.-H.; Cheng, C.-C.; Yang, C.-W.; Wei, K.-H.; Yang, Y.; Wang, Y.; Sokaras, D.; Nordlund, D.; Yang, P.; Muller, D. A.; Chou, M.-Y.; Zhang, X.; Li, L.-J., Janus Monolayers of Transition Metal Dichalcogenides. *Nat. Nanotechnol.* **2017,** *12*, 744-749.

(47) Zhang, J.; Jia, S.; Kholmanov, I.; Dong, L.; Er, D.; Chen, W.; Guo, H.; Jin, Z.; Shenoy, V. B.; Shi, L.; Lou, J., Janus Monolayer Transition-Metal Dichalcogenides. *ACS Nano* **2017,** *11* (8), 8192-8198.

(48) Sheng, Y.; Tan, H.; Wang, X.; Warner, J. H., Hydrogen Addition for Centimeter-Sized Monolayer Tungsten Disulfide Continuous Films by Ambient Pressure Chemical Vapor Deposition. *Chem. Mater.* **2017,** *29* (11), 4904-4911.

(49) Chen, T.; Zhou, Y.; Sheng, Y.; Wang, X.; Zhou, S.; Warner, J. H., Hydrogen-Assisted Growth of Large-Area Continuous Films of MoS_2 on Monolayer Graphene. *ACS Appl. Mater. Interfaces* **2018,** *10* (8), 7304-7314.

(50) Lu, Y.; Chen, T.; Ryu, G. H.; Huang, H.; Sheng, Y.; Chang, R.-J.; Warner, J. H., Self-Limiting Growth of High-Quality 2D Monolayer MoS_2 by Direct Sulfurization Using Precursor-Soluble Substrates for Advanced Field-Effect Transistors and Photodetectors.

ACS Appl. Nano Mater. **2019,** *2* (1), 369-378.

(51) Sasaki, S.; Kobayashi, Y.; Liu, Z.; Suenaga, K.; Maniwa, Y.; Miyauchi, Y.; Miyata, Y., Growth and Optical Properties of Nb-Doped WS_2 Monolayers. *Appl. Phys. Express* **2016,** *9* (7), 071201.

(52) Mouri, S.; Miyauchi, Y.; Matsuda, K., Tunable Photoluminescence of Monolayer MoS_2 via Chemical Doping. *Nano Lett.* **2013,** *13* (12), 5944-5948.

(53) Robertson, A. W.; Lin, Y.-C.; Wang, S.; Sawada, H.; Allen, C. S.; Chen, Q.; Lee, S.; Lee, G.-D.; Lee, J.; Han, S.; Yoon, E.; Kirkland, A. I.; Kim, H.; Suenaga, K.; Warner, J. H., Atomic Structure and Spectroscopy of Single Metal (Cr, V) Substitutional Dopants in Monolayer MoS_2. *ACS Nano* **2016,** *10* (11), 10227-10236.

(54) Sevy, A.; Huffaker, R. F.; Morse, M. D., Bond Dissociation Energies of Tungsten Molecules: WC, WSi, WS, WSe, and WCl. *J. Phys. Chem. A* **2017,** *121* (49), 9446-9457.

(55) Drowart, J.; Goldfinger, P., The Dissociation Energies of the Group VIA Diatomic Molecules. *Q. Rev. Chem. Soc.* **1966,** *20* (4), 545-557.

(56) Ji, H. G.; Lin, Y.-C.; Nagashio, K.; Maruyama, M.; Solís-Fernández, P.; Sukma Aji, A.; Panchal, V.; Okada, S.; Suenaga, K.; Ago, H., Hydrogen-Assisted Epitaxial Growth of Monolayer Tungsten Disulfide and Seamless Grain Stitching. *Chem. Mater.* **2018,** *30* (2), 403-411.

TOC Graphic